Supplementary Information: "Bose-Einstein condensation of a two-magnon bound state in a spin-one triangular lattice"

Jieming Sheng,[1,2,*] Jia-Wei Mei,[1,3,4,†] Le Wang,[1,3,*] Wenrui Jiang,[1,3] Lei Xu,[5] Han Ge,[1] Nan Zhao,[1] Tiantian Li,[1] Andrea Candini,[6] Bin Xi,[7] Jize Zhao,[8,9] Ying Fu,[1,3] Jiong Yang,[10] Yuanzhu Zhang,[10] Giorgio Biasiol,[11] Shanmin Wang,[1] Jinlong Zhu,[1,2] Ping Miao,[12,13] Xin Tong,[12,13] Dapeng Yu,[3,1] Richard Mole,[14] Long Ma,[15] Zhitao Zhang,[15] Zhongwen Ouyang,[16] Wei Tong,[15] Andrey Podlesnyak,[17] Ling Wang,[5] Feng Ye,[17] Dehong Yu,[14,‡] Liusuo Wu,[1,4,§] and Zhentao Wang[18,19,5,¶]

[1]*Department of Physics, Southern University of Science and Technology, Shenzhen 518055, China*

[2]*Academy for Advanced Interdisciplinary Studies, Southern University of Science and Technology, Shenzhen, 518055, China*

[3]*Shenzhen Institute for Quantum Science and Engineering, Shenzhen 518055, China*

[4]*Shenzhen Key Laboratory of Advanced Quantum Functional Materials and Devices, Southern University of Science and Technology, Shenzhen 518055, China*

[5]*School of Physics, Zhejiang University, Hangzhou 310058, China*

[6]*Advanced Materials Unit, Istituto Sintesi Organica e Fotoreattività ISOF - CNR Via P. Gobetti, 101 - 40129 Bologna*

[7]*College of Physics Science and Technology, Yangzhou University, Yangzhou 225002, China*

[8]*School of Physical Science and Technology & Key Laboratory for Magnetism and Magnetic Materials of the MoE, Lanzhou University, Lanzhou 730000, China*

[9]*Lanzhou Center for Theoretical Physics and Key Laboratory of Theoretical Physics of Gansu Province, Lanzhou University, Lanzhou 730000, China*

[10]*Department of Chemistry, Southern University of Science and Technology, Shenzhen 518055, China*

[11]*IOM CNR, Laboratorio TASC, Area Science Park Basovizza, Trieste 34149, Italy*

[12]*Institute of High Energy Physics, Chinese Academy of Sciences (CAS), Beijing 100049, China*

[13]*Spallation Neutron Source Science Center (SNSSC), Dongguan 523803, China*

[14]*Australian Nuclear Science and Technology Organisation, Lucas Heights, New South Wales 2234, Australia*
[15]*Anhui Province Key Laboratory of Condensed Matter Physics at Extreme Conditions, High Magnetic Field Laboratory, Chinese Academy of Sciences, Hefei 230031, China*
[16]*Wuhan National High Magnetic Field Center and School of Physics, Huazhong University of Science and Technology, Wuhan 430074, China*
[17]*Neutron Scattering Division, Oak Ridge National Laboratory, Oak Ridge, Tennessee 37831, USA*
[18]*School of Physics and Astronomy, University of Minnesota, Minneapolis, Minnesota 55455, USA*
[19]*Center for Correlated Matter, Zhejiang University, Hangzhou 310058, China*
(Dated: June 16, 2023)

I. SINGLE CRYSTAL X-RAY DIFFRACTION REFINEMENTS

High quality single crystals of $Na_2BaNi(PO_4)_2$ were grown using the flux method, and the crystal structure of $Na_2BaNi(PO_4)_2$ was characterized using a Bruker D8 Quest diffractometer with Mo-Kα radiation ($\lambda = 0.71073$ Å). The data integration and reduction were performed with the commercial Bruker APEX2 software suite. The refined lattice parameters and the atomic occupations are presented in Tables S1 and S2. We note that a slightly different crystal structure with space group $P\bar{3}$ was reported [1, 2]. We also tried refining the crystal structure with $P\bar{3}$, but obtained higher R-factors: $R_1 = 6.57$, $\omega R_2 = 8.90$.

TABLE S1. Single crystal X-ray diffraction refinements for $Na_2BaNi(PO_4)_2$.

Formula	**$Na_2BaNi(PO_4)_2$**
Formula mass (g/mol)	431.95
Crystal system	Trigonal
Space group	$P\bar{3}m1$
a(Å)	5.2806(4)
b(Å)	5.2806(4)
c(Å)	6.9591(5)
α	90°
β	90°
γ	120°
V(Å^3)	168.054(5)
$T(K)$	100
$\rho(cal)(g/cm^3)$	4.269
λ(Å)	0.71073
F (000)	214.0
Crystal size (mm^3)	$0.11 \times 0.06 \times 0.02$
μ (mm^{-1})	17.454
Final R indices	$R_1 = 3.83$, $\omega R_2 = 5.95$
R indices (all data)	$R_1 = 3.98$, $\omega R_2 = 6.00$
Goodness of fit	2.97

TABLE S2. Wyckoff positions, coordinates, occupancies, and equivalent isotropic displacement parameters for $Na_2BaNi(PO_4)_2$.

Atom	**Wyckoff site**	*x*	*y*	*z*	**Occupancy**	U_{eq}
Ba_1	1*a*	0	0	0	1	0.00310
Ni_1	1*b*	0	0	0.5	1	0.00593
Na_1	2*d*	0.666667	0.333333	0.681298	1	0.01090
P_1	2*d*	0.666667	0.333333	0.243700	1	0.00556
O_1	2*d*	0.666667	0.333333	0.026836	1	0.00814
O_2	6*i*	0.356792	0.178396	0.323064	1	0.03942

II. MAGNETIZATION MEASUREMENTS

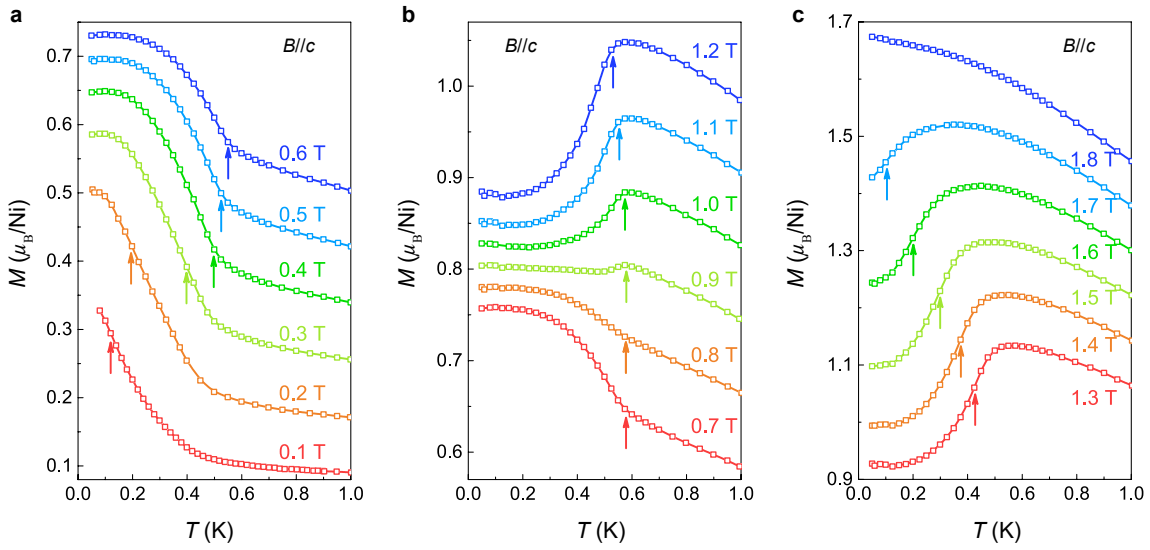

FIG. S1. Temperature dependent magnetization of $Na_2BaNi(PO_4)_2$ with field along the ***c*** axis. The arrows indicate the transition temperatures at different fields.

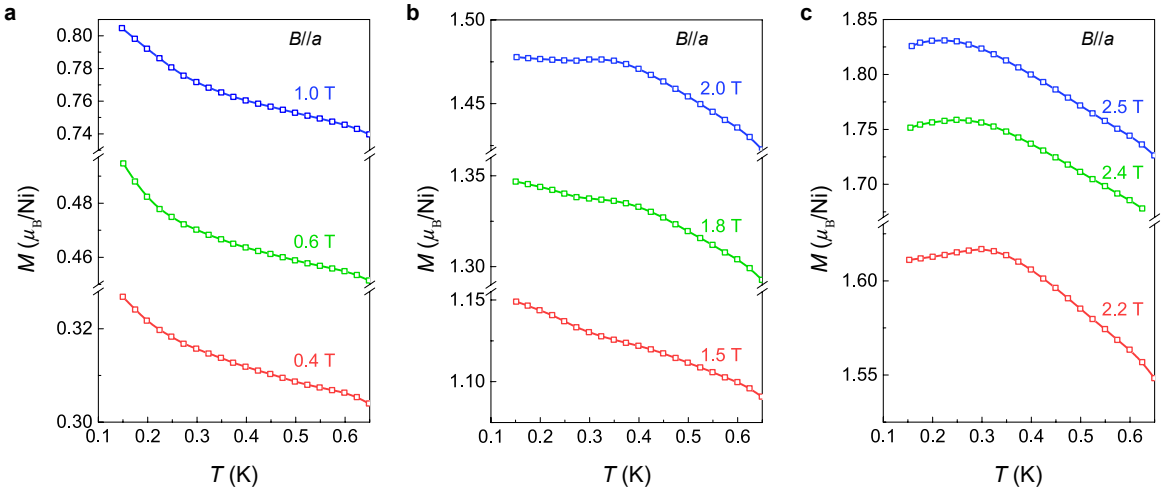

FIG. S2. Temperature dependent magnetization of $Na_2BaNi(PO_4)_2$ with field in the ***ab*** plane.

The temperature dependent magnetization of $Na_2BaNi(PO_4)_2$ with field along the ***c*** and ***a*** axes are shown in Figs. S1 and S2, respectively. All the transition temperatures were determined through the peak positions of the temperature derivative dM/dT, indicated by the arrows shown in Fig. S1.

Figure S3**a**-**b** show the isothermal magnetization $M(B)$ measured at various temperatures with $B \parallel \boldsymbol{c}$ and $B \parallel \boldsymbol{a}$, respectively. As we lower the temperature, the phase boundaries gradually become

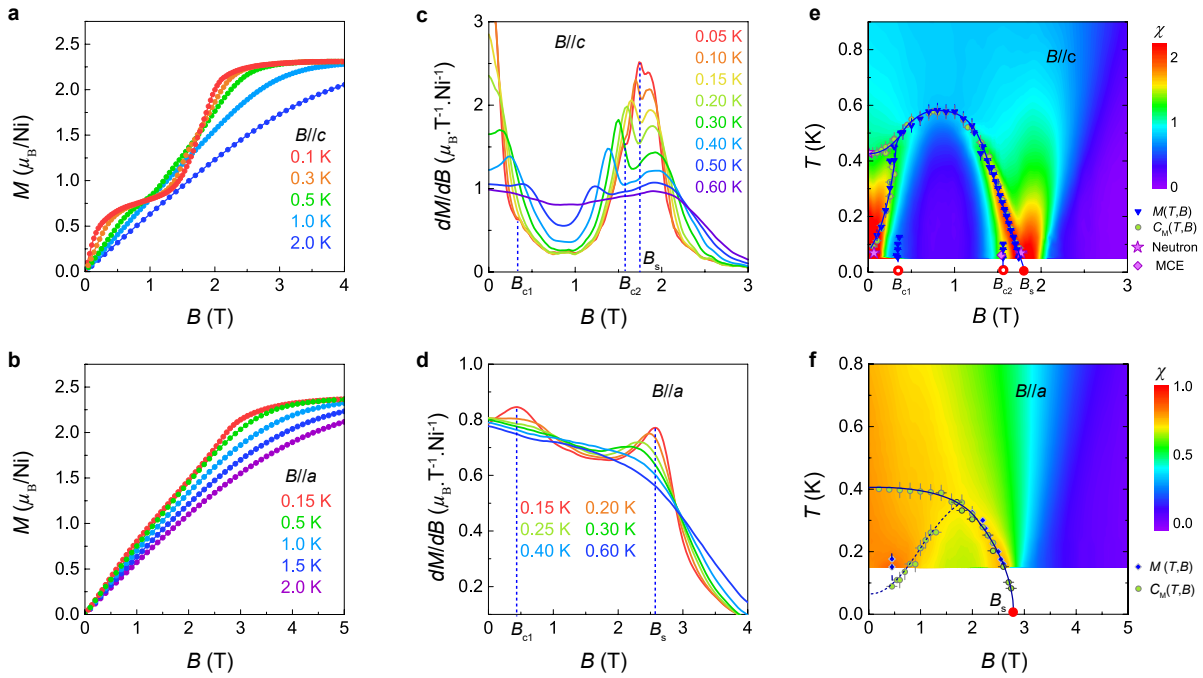

FIG. S3. **a**-**b** Field dependence of magnetization $M(B)$ measured at different temperatures with field applied along the ***c*** and ***a*** axes, respectively. **c**-**d** Magnetic susceptibilities dM/dB measured at different temperatures with field applied along the ***c*** and ***a*** axes, respectively. **e**-**f** The field-temperature magnetic phase diagram overlaid on the contour plots of magnetic susceptibility dM/dB with magnetic field along the ***c*** and ***a*** axes, respectively. The magnetic phase boundaries were extracted through $M(T,B)$, $C(T,B)$, neutron diffraction and MCE measurements.

pronounced for both field directions. For $B \parallel \boldsymbol{c}$, a broad plateau at about one third of the saturated moment is revealed for $T \lesssim 0.3\,\mathrm{K}$. In contrast, no plateau phase was observed for field in the ***ab*** plane. The temperature evolution of the anomalies in dM/dB curves for both field directions are illustrated in Figs. S3**c**-**d**. The contour plots of the magnetic susceptibility dM/dB as a function of temperature and field for both field directions are presented in Figs. S3**e**-**f**. The Magnetic phase boundaries extracted through $M(T,B)$, $C(T,B)$, neutron diffraction and magnetocaloric effect (MCE) measurements are over-plotted.

III. SPECIFIC HEAT MEASUREMENTS

The low-temperature specific heat of $Na_2BaNi(PO_4)_2$ with magnetic field applied along the ***c*** and ***a*** axes are shown in Figs. S4-S5, respectively. For both field directions, clear sharp anomalies were observed and the peak positions were extracted as the upper phase boundaries, shown as circles in Fig. 2**e** in the main text and Figs. S3**e**-**f** in Supplementary Information.

The magnetic phase diagrams overlaid on the contour plots of normalized entropy $S/R\ln 3$ for both field directions are shown in Fig. S6. It is clear that only a small portion of the full $R\ln 3$ entropy is released (about $0.2R\ln 3$ to $0.4R\ln 3$) at the upper phase boundary. In other words, a great amount of moments are still fluctuating deep inside these ordered phases.

Since spin fluctuations persist down to the inaccessible low-temperature region, we have extrapolated a residual entropy of $0.15R\ln 3$ at $B = 0$ in the main text. Note that the spin fluctuations are greatly reduced in the 1/3-plateau (see Fig. S6**a**), as a result the full $R\ln 3$ is expected to be recovered in this phase without accounting for the inaccessible low-temperature region. Figure S7

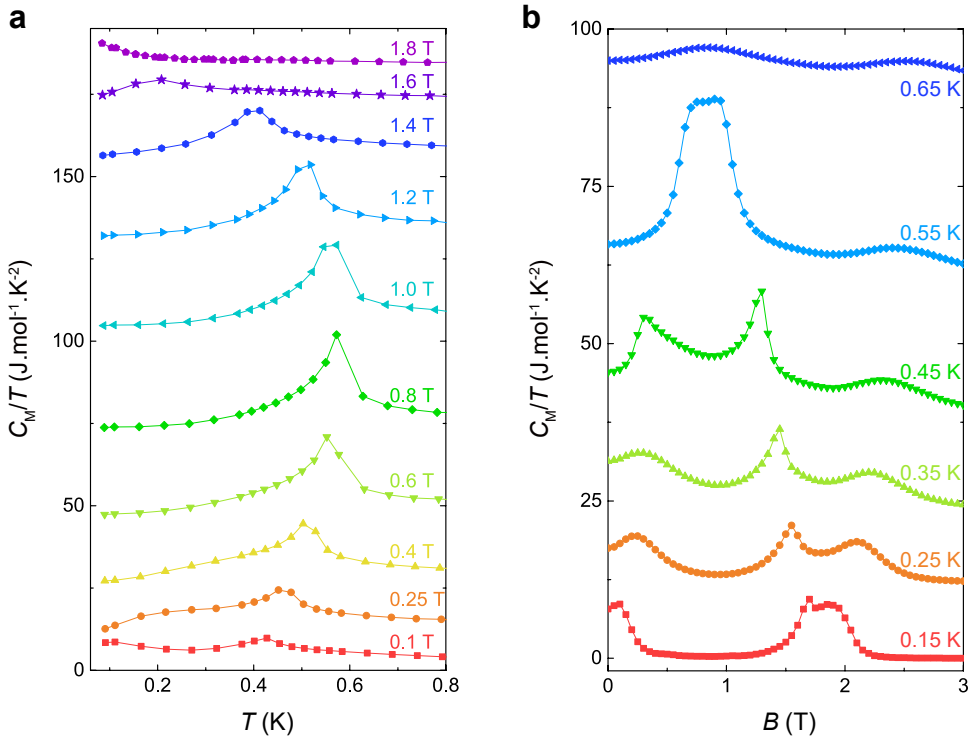

FIG. S4. **a** Temperature evolution of the magnetic specific heat C_M/T measured at different magnetic fields with $B \parallel \boldsymbol{c}$. **b** Field evolution of the magnetic specific heat C_M/T measured at different temperatures with $B \parallel \boldsymbol{c}$.

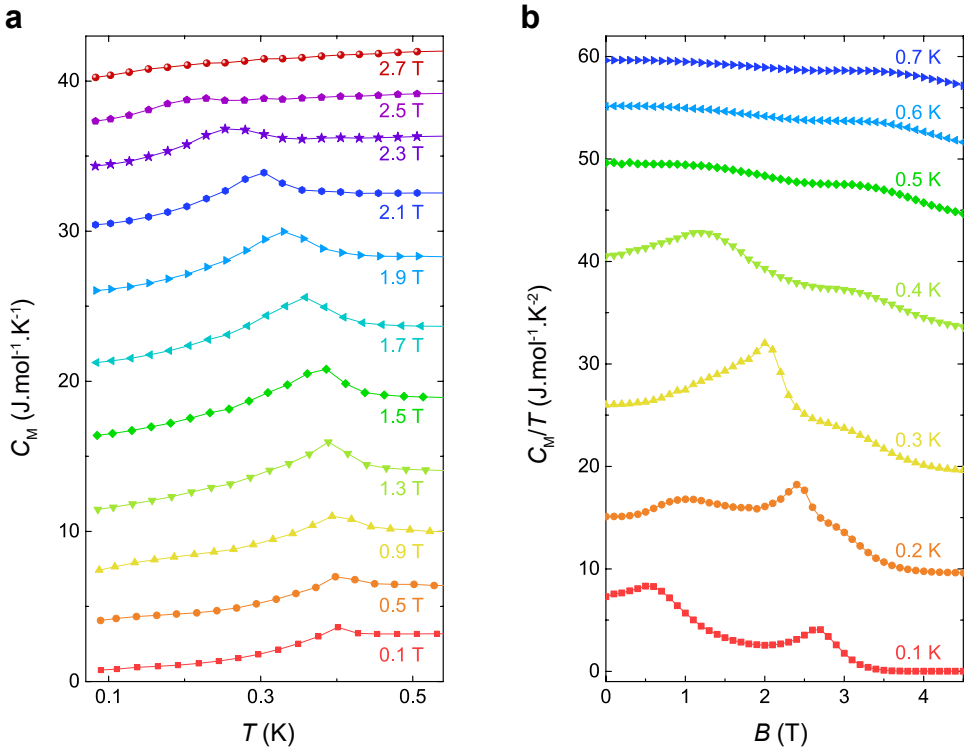

FIG. S5. **a** Temperature evolution of the magnetic specific heat C_{M} measured at different magnetic fields with $B \parallel \boldsymbol{a}$. **b** Field evolution of the magnetic specific heat C_{M}/T measured at different temperatures with $B \parallel \boldsymbol{a}$.

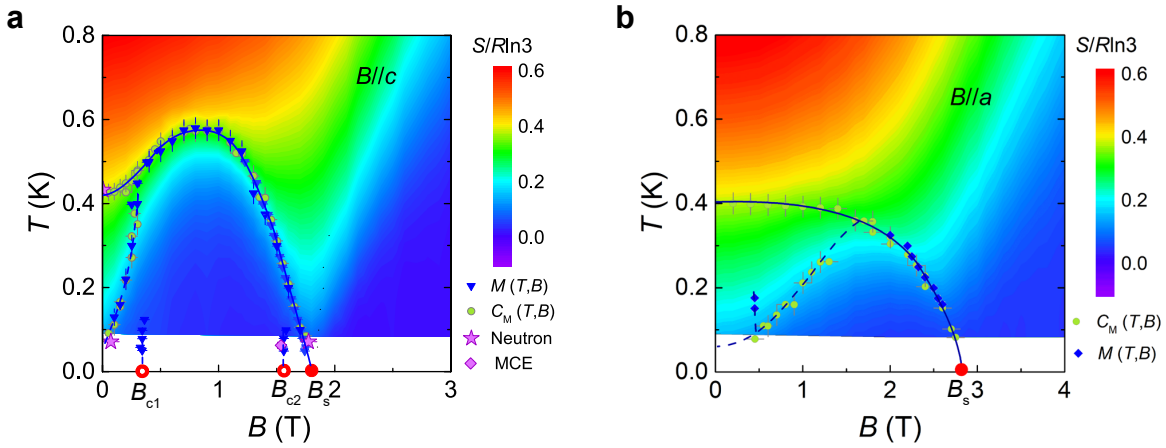

FIG. S6. The field-temperature magnetic phase diagram overlaid on the contour plots of the normalized entropy $S/R\ln 3$, with $B \parallel \boldsymbol{c}$ and $B \parallel \boldsymbol{a}$, respectively. The magnetic phase boundaries were extracted through $M(T,B)$, $C(T,B)$, neutron diffraction and MCE measurements.

shows the temperature dependent magnetic specific heat (blue filled circles) measured at $B = 0.8\,\mathrm{T}$.

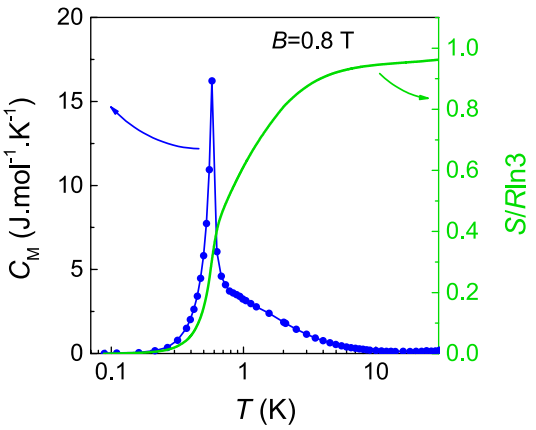

FIG. S7. Left axis: Temperature dependence of the magnetic specific heat (blue filled circles) measured at $B = 0.8\,\mathrm{T}$ with $B \parallel \boldsymbol{c}$. Right axis: The temperature dependence of the integrated magnetic entropy at $B = 0.8\,\mathrm{T}$ (green solid line).

The corresponding integrated entropy (green soild line) is also presented, without adding a residual entropy by hand. We can find the total entropy reaches $0.96R\ln 3$ above 10 K, clearly demonstrating the effective spin-1 physics for $Na_2BaNi(PO_4)_2$.

IV. MAGNETIC STRUCTURE ANALYSIS

The magnetic structure of $Na_2BaNi(PO_4)_2$ at 80 mK was analyzed by representation theory. For Ni site at (0,0,0.5) and the magnetic propagation vector (1/3, 1/3, $k_c = \pm 0.293(1)$), the spin configuration can be described by three different irreducible representations (IRs). Table S3 lists the basis vectors for IRs Γ_1, Γ_2 and Γ_3, respectively.

For Γ_1, the moments are constrained along the $\boldsymbol{c}$ axis with an "UUD" spin configuration in the $\boldsymbol{ab}$ plane (Fig. S8**a**). The amplitude of the moment is modulated by $e^{ik_c \cdot r_c}$ along the $\boldsymbol{c}$-axis. For

TABLE S3. Basis vectors of decomposed irreducible representations (IR) of space group $P\bar{3}m1$ with magnetic wave-vector $\boldsymbol{k} = (1/3, 1/3, 0.293)$ and moments on Ni site (0,0,0.5).

IR	m_a	m_b	m_c	im_a	im_b	im_c
Γ_1	0	0	1	0	0	0
Γ_2	1	0	0	0.5774	1.1547	0
Γ_3	1	0	0	-0.5774	-1.1547	0

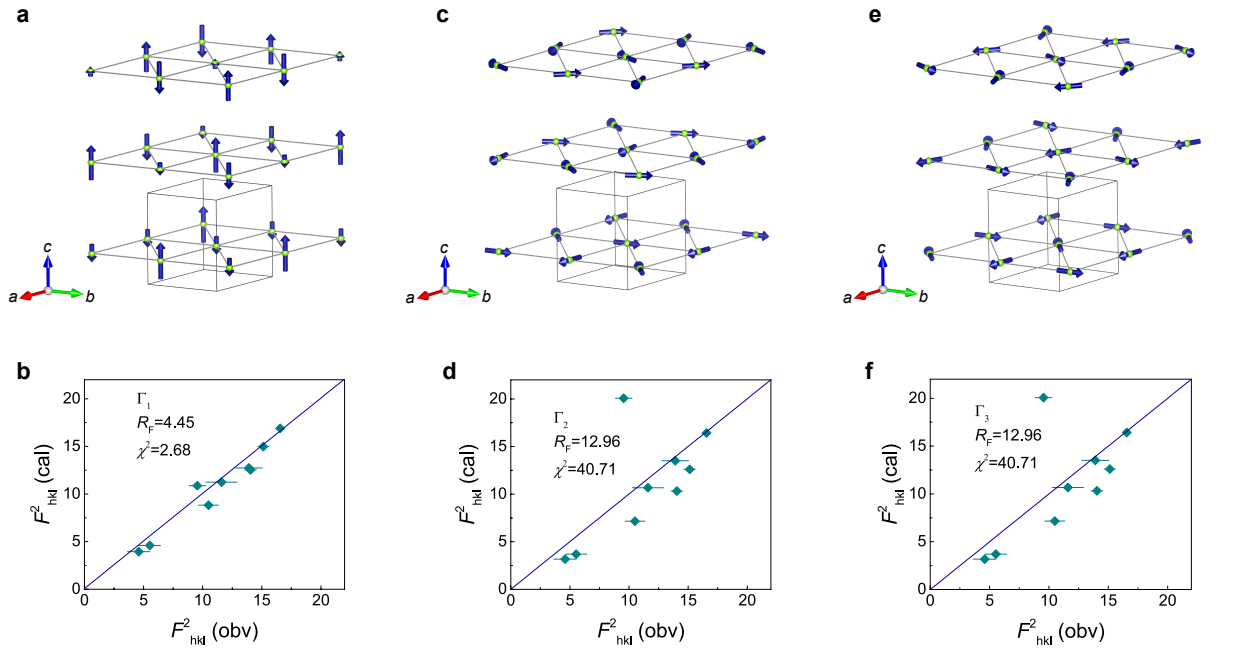

FIG. S8. **a**, **c** and **e** Possible zero-field magnetic structures of $Na_2BaNi(PO_4)_2$ correspond to three different IRs Γ_1, Γ_2 and Γ_3, respectively. **b**, **d** and **f** The calculated magnetic structure factor versus observation using Γ_1, Γ_2 and Γ_3 model, respectively.

Γ_2 and Γ_3, the magnetic structures are degenerate 120° spin structures with anti-phase chirality. The moments rotate along the $\boldsymbol{c}$-axis with an angle $\cos^{-1}(k_c \cdot r_c)$, as shown in Figs. S8**c** and **e**, respectively. By Rietveld refinement, we found that Γ_1 gives the best fit with $R_F = 4.45$, $\chi^2 = 2.68$ for the single crystal neutron diffraction data measured 80 mK and 0 T, as shown in Fig. S8**b**.

V. SCALING ANALYSIS OF THE PHASE BOUNDARY

The scaling analysis of the exponents should be performed in a low-temperature window [3, 4]. To verify the exponents extracted in this work are robust and valid, we tried to fit them for a series of window sizes to check convergence. In Fig. S9, we show that νz stays practically at 1 across a wide range of fitting windows: from $T_{\max} \approx 374.1\,\mathrm{mK} \sim 0.65 T_{\mathrm{c\,max}}$ down to $T_{\max} \approx 124.2\,\mathrm{mK}$, confirming that the fitting is robust in a wide critical region.

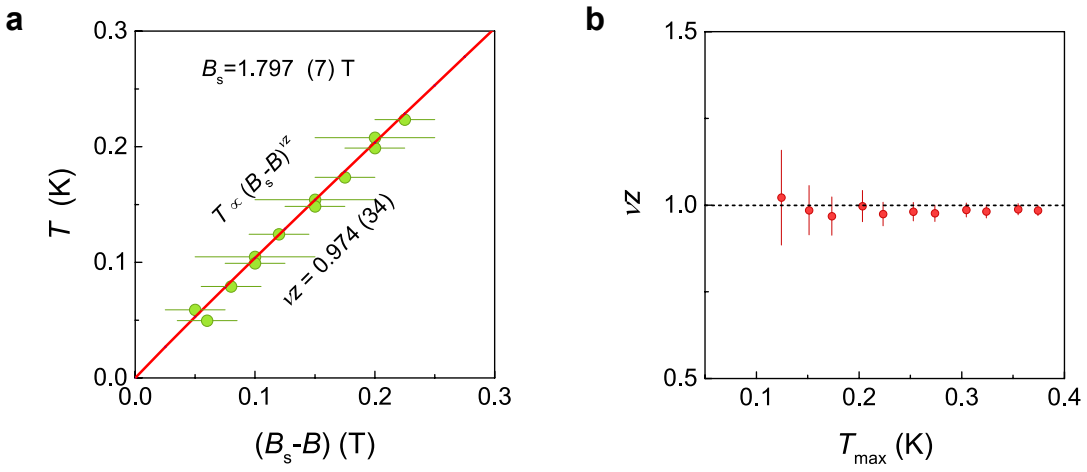

FIG. S9. **a** Scaling behavior of the magnetic phase boundary $T \propto (B_{\mathrm{s}} - B)^{\nu z}$ with the highest temperature of fitting range $T_{\max}$=223.4 mK $\lesssim 0.4 T_{c\ \max}$ in the vicinity the critical field B_{s}. **b** Critical exponents νz as a function of $T_{\max}$, with fitting performed for 49.5 mK $\leq T \leq T_{\max}$.

VI. NEUTRON SCATTERING

Figure S10**a**-**b** shows the temperature evolution of magnetic reflections $(-\frac{2}{3},\frac{1}{3},L)$ at zero field. As the temperature rises from 80 mK, the absolute value of the L component dramatically decreases (solid blue dots), indicating it is near the border of a phase transition. In this zero-field case, we did not reach lower temperature to fully pin down the transition, similar to the other thermodynamic measurements, indicating that T_{N1} is slightly below 80 mK. Further increasing the temperature, the L location of the magnetic reflections remains basically unchanged, while the intensity of the magnetic peaks gradually decreases. The dashed black arrow around 431 mK, shown in Fig. S10**b**,

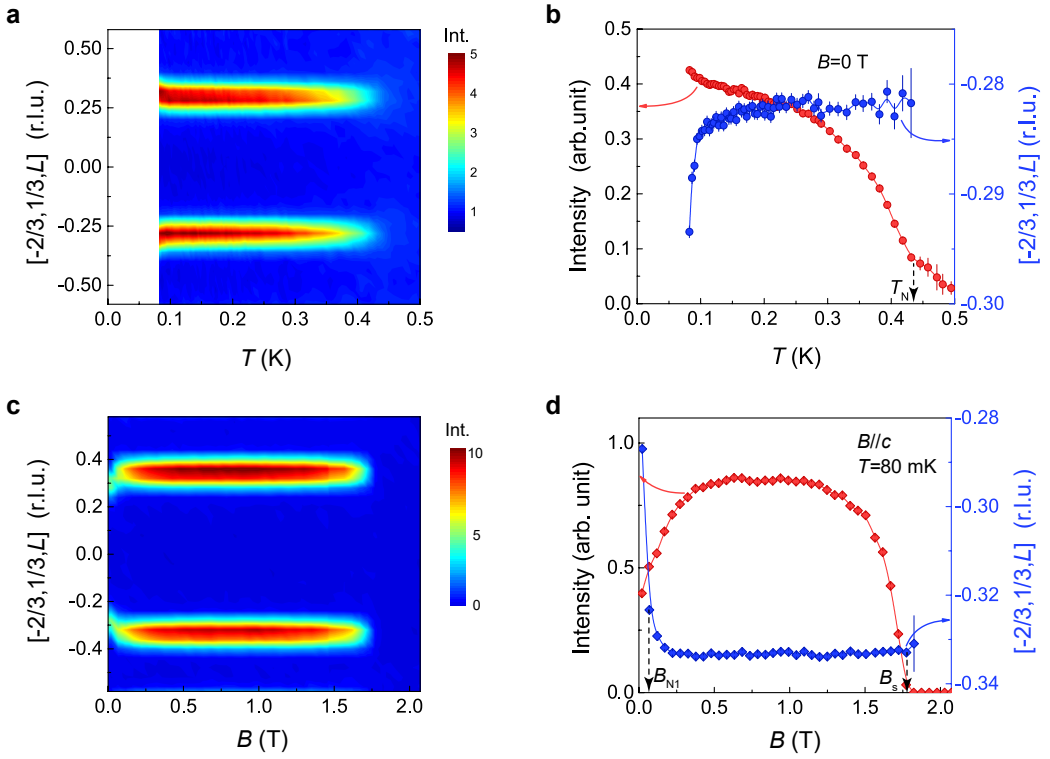

FIG. S10. **a** Contour plot of temperature evolution of the magnetic reflections at $(-\frac{2}{3},\frac{1}{3},L)$ measured at zero field. **b** The line cuts of temperature evolution of the incommensurate magnetic reflections $(-\frac{2}{3},\frac{1}{3},L)$ measured at zero field. The red and blue filled circles represent the integrated intensity and the L component of the magnetic reflection, respectively. **c** The contour plot of field evolution of the magnetic reflections at $(-\frac{2}{3},\frac{1}{3},L)$ measured at $T = 80$ mK. **d** The line cuts of field evolution of the incommensurate magnetic reflections $(-\frac{2}{3},\frac{1}{3},L)$ measured at $T = 80$ mK. The red and blue diamonds represent the integrated intensity and the L component of the magnetic reflection, respectively.

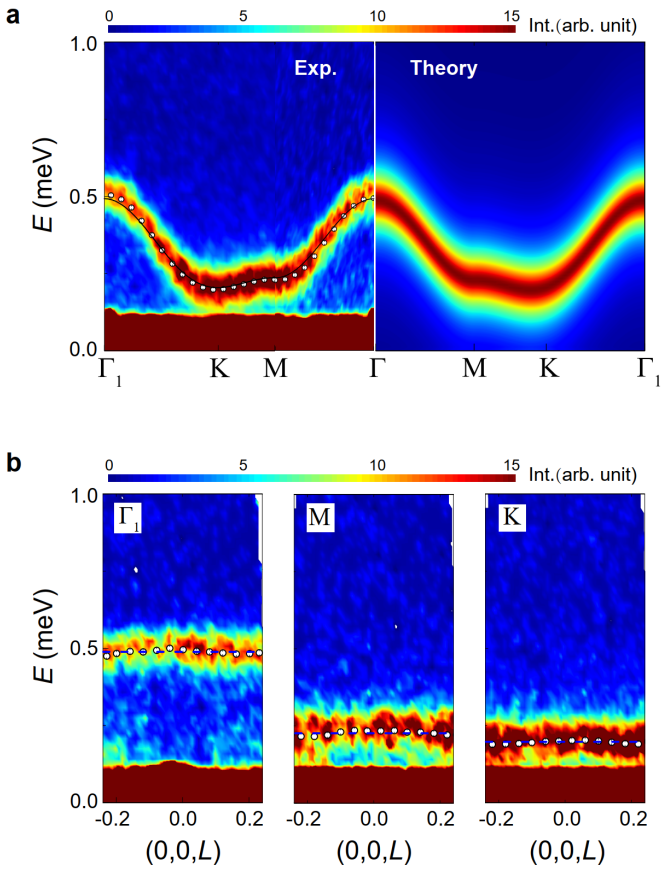

FIG. S11. **a** Inelastic neutron scattering intensity measured at $T = 60\,\mathrm{mK}$ and $B = 3\,\mathrm{T}$ along different high symmetry directions using incident neutron energy $E_\mathrm{i} = 3.3\,\mathrm{meV}$. The intensity is integrated over the window of $L = [-0.22, 0.22]$. The black empty circles are centers of the Gaussian fit to the data. The theoretical 1-magnon dispersion (black solid line on the left) and intensity (contour map on the right) used the same parameters as in Fig. 3**c** in the main text, except that here we use $B = 3\,\mathrm{T}$ instead of $B = 5\,\mathrm{T}$. **b** Inelastic neutron scattering intensity along L-direction for different in-plane momenta at $T = 60\,\mathrm{mK}$ and $B = 3\,\mathrm{T}$. The black empty circles are centers of the Gaussian fit to the data and the blue dashed lines are guides to the eye.

corresponds to the AFM phase transition at T_N. For $T > T_\mathrm{N}$, we can still observe the weak diffuse scattering along the $\boldsymbol{c}$ axis, resulting in the residual intensity as seen in Fig. S10**b**.

To reveal the location of T_N1, we followed the same strategy as the other thermodynamic measurements performed in this work. By applying a magnetic field along the $\boldsymbol{c}$ axis, we indeed see that the L component of the magnetic reflections undergoes an abrupt change to 1/3 (Fig. S10**c**-**d**), confirming that T_{N1} is an incommensurate-commensurate transition, and for $T_{N1} = 80\,\mathrm{mK}$ the corresponding critical field B_{N1} is tiny (see the left arrow in Fig. S10**d**). As the field is further

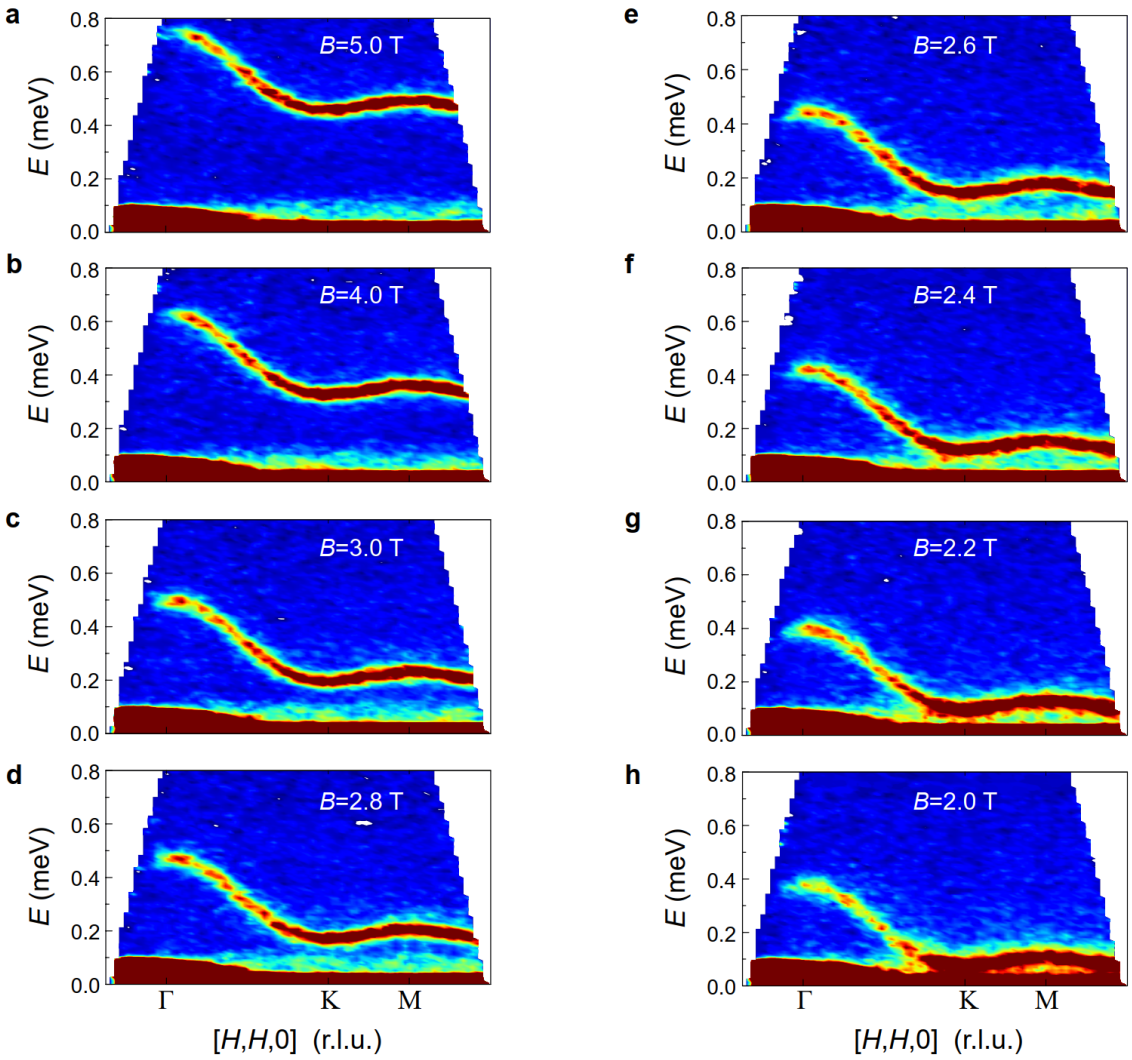

FIG. S12. The inelastic neutron scattering spectra along the high-symmetry directions measured at $T = 60\,\mathrm{mK}$ and **a** $B = 5.0\,\mathrm{T}$, **b** $B = 4.0\,\mathrm{T}$, **c** $B = 3.0\,\mathrm{T}$, **d** $B = 2.8\,\mathrm{T}$, **e** $B = 2.6\,\mathrm{T}$, **f** $B = 2.4\,\mathrm{T}$, **g** $B = 2.2\,\mathrm{T}$, **h** $B = 2.0\,\mathrm{T}$. The intensity is integrated over the window of $L = [-0.22, 0.22]$. The incident neutron energy $E_\mathrm{i} = 1.5\,\mathrm{meV}$ is used here.

raised, the intensity of the magnetic peak reaches the maximum in the center of the 1/3-plateau until it is suppressed at the saturation field $B_\mathrm{s} \approx 1.8\,\mathrm{T}$. Note that we did not observe the transition $B_{\mathrm{c}2} \approx 1.56\,\mathrm{T}$ in the neutron diffraction data, while both the magnetization and MCE data clearly indicate its existence, possibly related to the first order nature of the $B_{\mathrm{c}2}$ transition. Another possibility is that our sample was heated up by the neutrons, pushing it outside the SN phase. Further investigations are in our plan to clear up this issue.

Figure S11**a** shows the inelastic neutron scattering spectrum along different high-symmetry directions measured at $T = 60\,\mathrm{mK}$ and $B = 3\,\mathrm{T}$ with the field applied along the $\boldsymbol{c}$-axis. By using the same parameters as in Fig. 3**c** in the main text, the theoretical 1-magnon dispersion (black solid line on the left) and intensity (contour map on the right) well reproduced the observed spin wave.

Figure S12 shows the inelastic neutron scattering spectra measured at different magnetic fields in the fully polarized state at $T = 60\,\mathrm{mK}$ using $E_\mathrm{i} = 1.5\,\mathrm{meV}$. By decreasing the magnetic field, the one-magnon spin wave gradually moved to lower energies.

VII. MAGNETOCALORIC EFFECT (MCE)

As shown in Fig. S13, the MCE measurements show additional evidence of the transition at B_{c2}. By sweeping the magnetic field with a fixed bath temperature $T = 50\,\mathrm{mK}$, the sample temperature variation was recorded as the field was swept through the phase boundaries. It is clear that the value of B_{c2} determined from dM/dB agrees well with the anomaly observed in the MCE curves (Fig. S13**a**-**b**). To further verify the transition at B_{c2}, the MCE measurements were repeated at three different samples. As illustrated in Fig. S13**c**-**e**, the anomaly at B_{c2} can be observed in all three samples.

Furthermore, the B_{c2} anomaly shows a clear temperature dependence in both magnetization and MCE measurements. As shown in Fig. S14, we can find that the B_{c2} anomaly in dM/dB and MCE curves gradually disappears as we raise the temperature.

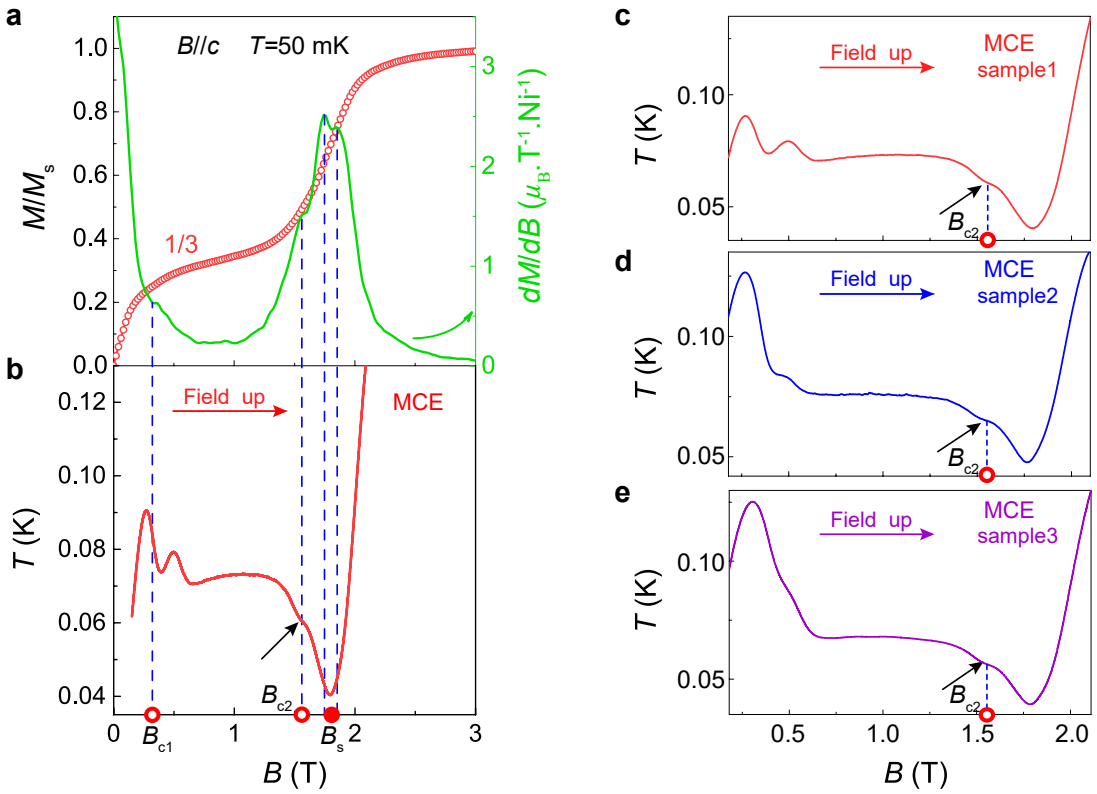

FIG. S13. **a** Magnetization and magnetic susceptibility dM/dB measured at 50 mK with the field applied along the ***c*** axis. **b** MCE measured by monitoring T while sweeping magnetic field up with a fixed bath temperature $T = 50\,\mathrm{mK}$ and the field applied along the ***c*** axis. **c**-**e** MCE measured at three different samples with a fixed bath temperature $T = 50\,\mathrm{mK}$ and magnetic field along the ***c*** axis.

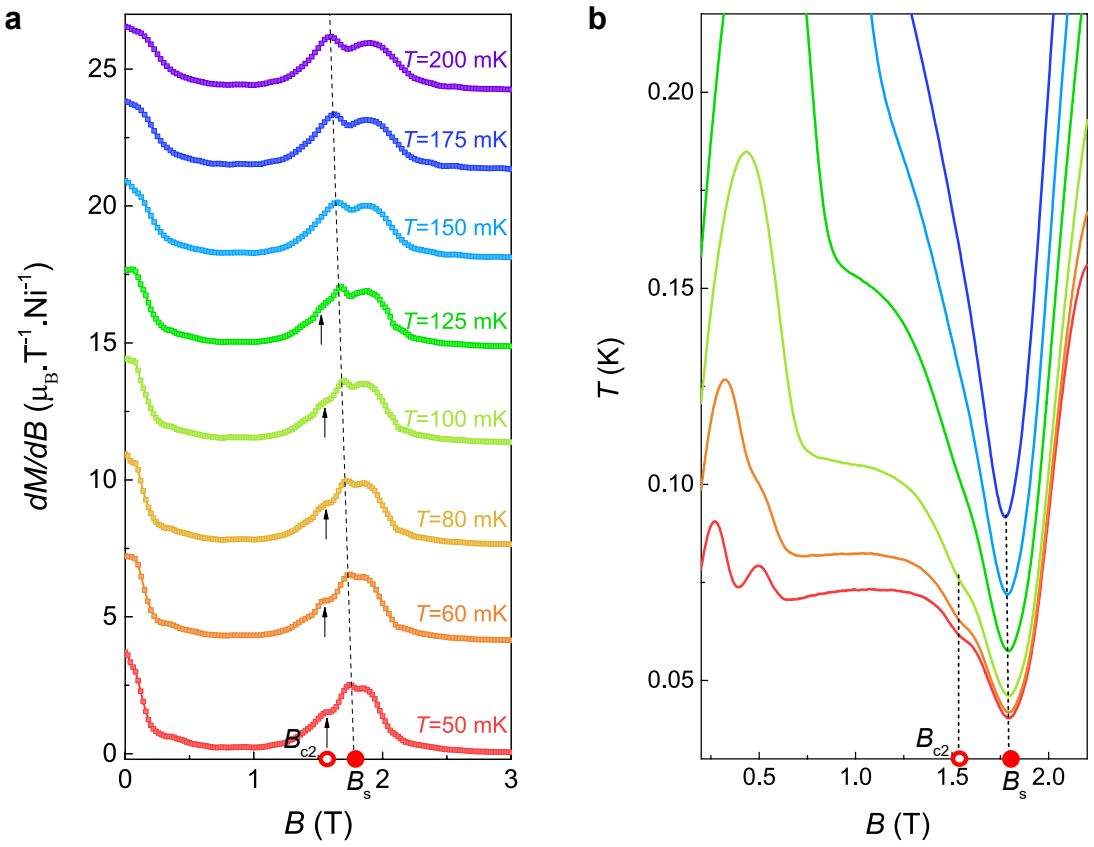

FIG. S14. **a** Magnetic susceptibility dM/dB measured at different temperatures with magnetic field along the ***c*** axis. **b** MCE measured by fixing different bath temperatures with magnetic field along the ***c*** axis.

VIII. ESR SPECTRA

As shown in Figure S15**a** and **b**, our earlier ESR measurements were carried out in a pulsed magnetic field at $T = 2$ K with $B \parallel \boldsymbol{ab}$ and $B \parallel \boldsymbol{c}$, respectively. Resonance peaks from 1-magnon excitation at Γ point marked by the black arrows are observed at different frequencies for both field directions. The corresponding frequency-field ($F - B$) relations for $B \parallel \boldsymbol{c}$ and $B \parallel \boldsymbol{ab}$ are shown in Fig. S15**c**. By linear fittings, we can get the g-factors $g_c = 2.25(1)$ and $g_{ab} = 2.24(5)$ (corrected by the measured g_{DPPH}), respectively.

Due to the noisy signals in our pulsed-field ESR spectra, we did not observe the weak 2-magnon bound state there. Later, we performed another ESR experiment in a steady magnetic field, where the magnetic field was tilted 6° away from the $\boldsymbol{c}$ axis. With the first-derivative collecting mode, higher quality data revealed more details in the steady-field ESR spectra. Figure S16 shows the ESR spectra of $Na_2BaNi(PO_4)_2$ measured in a steady magnetic field at $T = 2$ K. Besides the 1-magnon excitations at Γ point (indicated by the red arrows in Fig. S16), we can also observe the weak signals of the 2-magnon bound state at Γ point (blue arrows at lower field) and the finite-T excitations from the 1-magnon state to the 2-magnon bound state at K point (purple arrows at higher field). The specific excitation paths are also illustrated in Fig. S17**a**. We note that there are

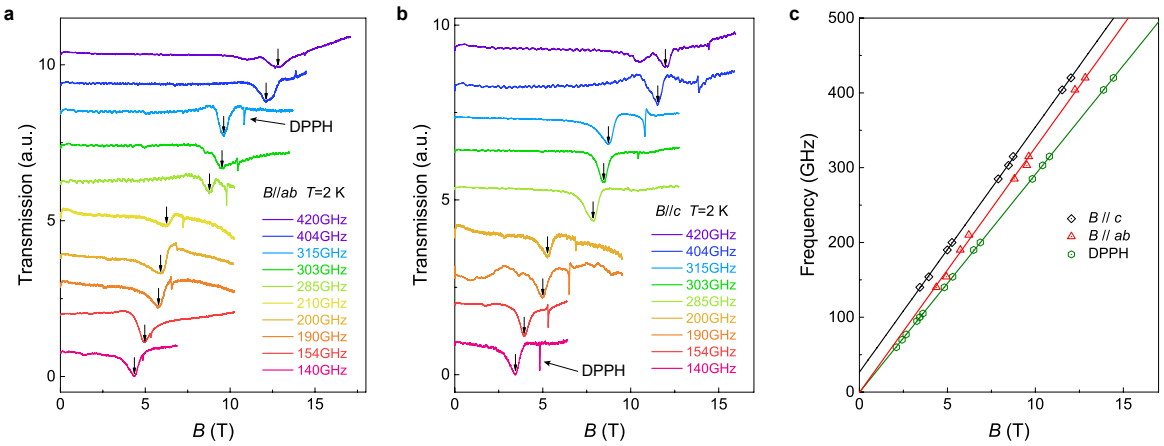

FIG. S15. **a** and **b** ESR spectra measured at $T = 2$ K in a pulsed magnetic field for $B \parallel \boldsymbol{ab}$ and $B \parallel \boldsymbol{c}$, respectively. The signals marked by the black arrows are from 1-magnon excitation at the Γ point, and the sharp anomalies in the ESR spectra are the resonant signals for DPPH. **c** The frequency-field relation obtained at $T = 2$ K with $B \parallel \boldsymbol{ab}$ (red triangles) and $B \parallel \boldsymbol{c}$ (black diamonds). The green hexagons are the ESR signals of DPPH.

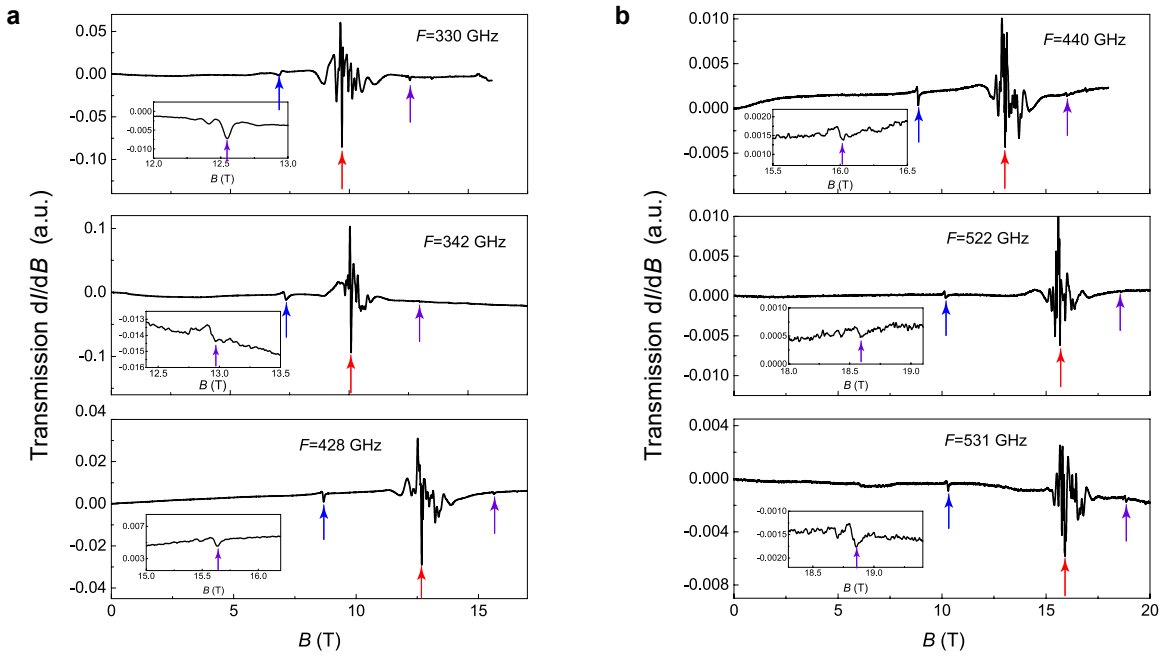

FIG. S16. ESR spectra measured at $T = 2\,\mathrm{K}$ in a steady magnetic field tilted 6° away from the $\boldsymbol{c}$ axis. The signals marked by the red, blue and purple arrows represent the 1-magnon excitation at Γ point, 2-magnon bound state at Γ point, and the finite-T excitation from the 1-magnon state to the 2-magnon bound state at K point, respectively. The insets show zoomed-in view of the excitation at higher field (purple arrow).

also a series of resonance signals around the 1-magnon resonance peaks, possibly correspond to the finite-T excitations from the 1-magnon state to the 2-magnon continuum.

The lines in Fig. S17**b** are the calculated $F - B$ relation of the 1-magnon state (red solid line) and the 2-magnon bound state (blue dashed line) at Γ point, and the finite-T excitation from the 1-magnon state to the 2-magnon bound state at K point (purple dashed line), with $B \parallel \boldsymbol{c}$. The red diamonds and the black circles are the ESR signals with $B \parallel \boldsymbol{c}$ (pulsed) and B tilted 6° away from the $\boldsymbol{c}$ axis (steady), respectively.

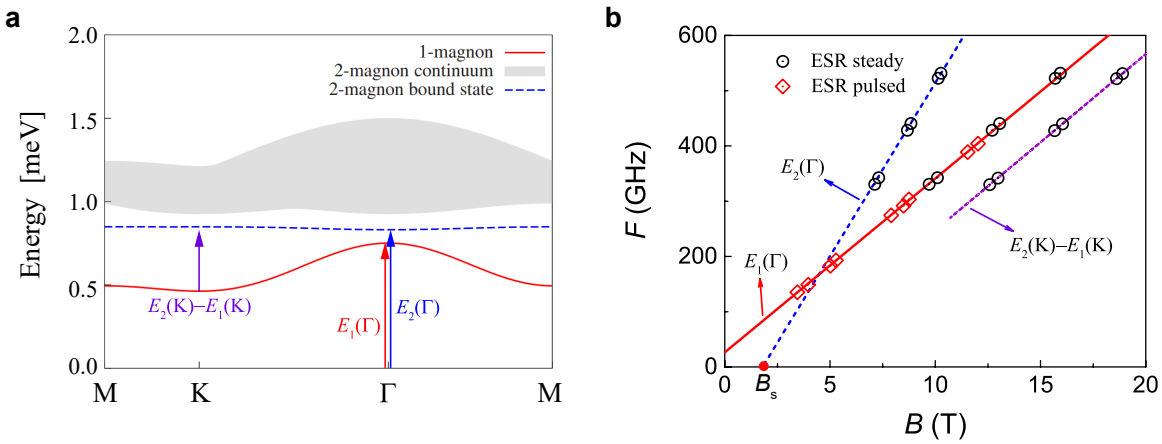

FIG. S17. **a** The energies of the 1-magnon excitation, 2-magnon continuum and 2-magnon bound state at $B = 5\,\mathrm{T}$, for the TL model (4) in the main text with $J = 0.032\,\mathrm{meV}$, $\Delta = 1.13$, $D/J = 3.97$, and $g_c = 2.24$. The arrows illustrate the dominant signals observed in our ESR experiments. **b** The calculated frequency-field relation of the 1-magnon state (red solid line) and the 2-magnon bound state (blue dashed line) at Γ point, and the finite-T excitation from the 1-magnon state to the 2-magnon bound state at K point (purple dashed line), with $B \parallel \boldsymbol{c}$. The red diamonds and black circles are the observed ESR signals with $B \parallel \boldsymbol{c}$ (pulsed) and B tilted 6° away from the $\boldsymbol{c}$-axis (steady), respectively.

IX. 3- AND 4-MAGNON STATES

To exclude the possibility of a first order transition at B_s, we check whether the 2-magnon bound states have attractive interactions, i.e., whether there are formation of 3- or 4-magnon bound states in the relevant parameter region. This can in principle be calculated exactly by solving the Lippmann-Schwinger equation, similarly to the 2-magnon solution presented in the main text. However, this approach quickly becomes over complicated as we increase the magnon number. In this section, we use a different method that can be easily generalized to handle larger number of magnons. The method was initially proposed by Trugman to study the holes in high-temperature superconductors [5, 6], and was later generalized to other systems [7–9].

Here we outline the basic idea of the method. In the FP state, the excitations are gapped for $B > B_s$. As a consequence, the size of the excited states are controlled by the finite correlation length ξ. Motivated by this observation, we start by creating local excitations $|\varphi_i\rangle$ (see Fig. S18 for the choice of initial states) and project them to momentum space:

$$|\varphi_i(\boldsymbol{k})\rangle \equiv \frac{\hat{P}(\boldsymbol{k})|\varphi_i\rangle}{\sqrt{\langle\varphi_i|\hat{P}(\boldsymbol{k})|\varphi_i\rangle}}. \tag{S1}$$

Here $\hat{P}(\boldsymbol{k}) \equiv \frac{1}{N}\sum_{\boldsymbol{r}} e^{i\boldsymbol{k}\cdot\boldsymbol{r}}\hat{T}(\boldsymbol{r})$ is the projection operator. Then we apply the Hamiltonian $\mathcal{H}_{\rm TL}$ to $|\varphi_i(\boldsymbol{k})\rangle$ to generate new states that dress up $|\varphi_i(\boldsymbol{k})\rangle$. Systematic improvement of the variational space is achieved by repeating this process iteratively. Finally, we diagonalize $\mathcal{H}_{\rm TL}$ in the variational basis $\{\varphi_i(\boldsymbol{k})\}$ to obtain both energy and wave function of the excited states. Convergence of this approach can be checked by comparing the energies and the measured quantities at different iterations.

We start by showing that the variational approach indeed agrees with the exact results for the 2-magnon bound state. After $M = 3$ iterations from the total $S^z = N - 2$ initial basis (see Fig. S18**a**), the dimension of the variational space is expanded from $\mathcal{D} = 4$ to $\mathcal{D} = 31$. Figure S19**a** shows that the dispersion of the 2-magnon bound state practically agrees with the exact solution even at $M = 3$. In other words, the 2-magnon bound state occupies a relatively small spatial range. Similarly, the dispersion of the 3-magnon and 4-magnon states at $M = 8$ iteration are shown in Figs. S19**b** and **c**, respectively.

The minimum of the 3-magnon state is located at the K-point (Fig. S19**b**). The binding energy is defined by subtracting a 2-magnon bound state at Γ-point and a 1-magnon state at K-point:

$$E_3^B(\mathrm{K}) = [E_2(\Gamma) + E_1(\mathrm{K})] - E_3(\mathrm{K}). \tag{S2}$$

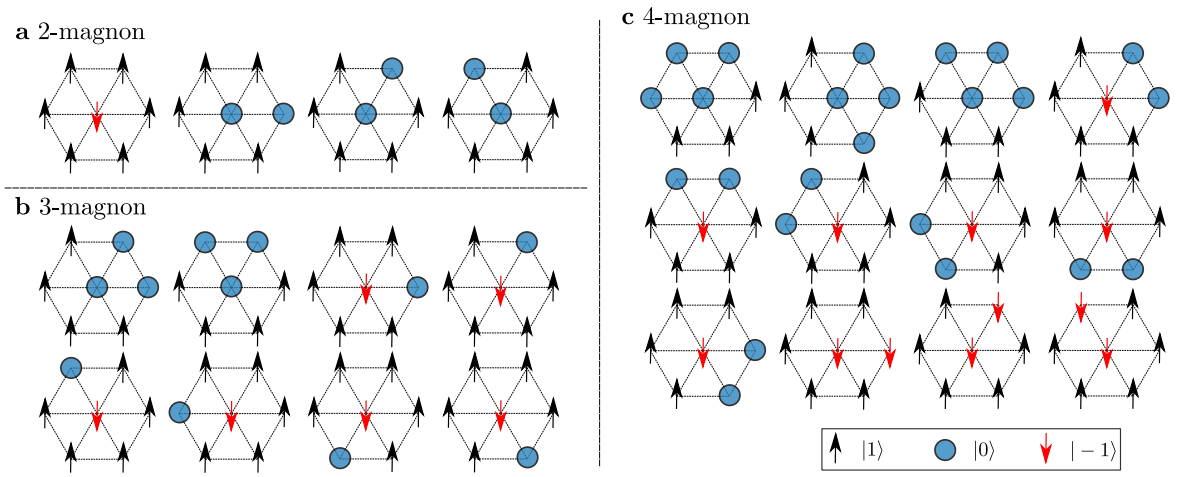

FIG. S18. **Initial basis for 2-, 3-, and 4-magnon states used in the variational method.**

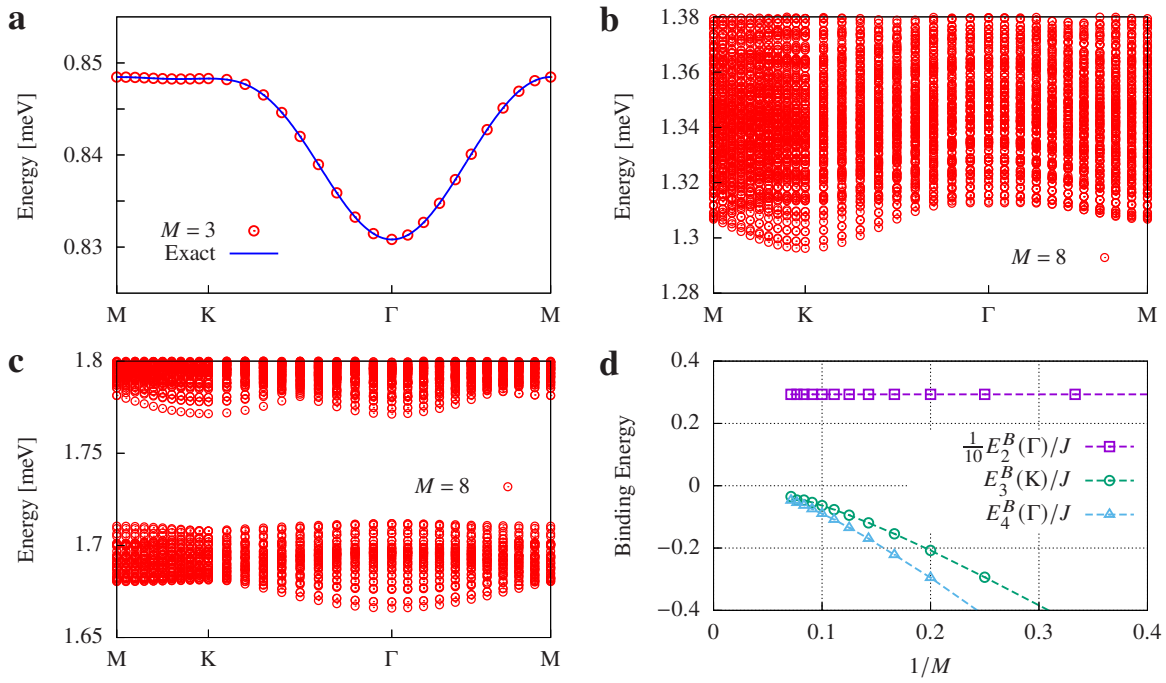

FIG. S19. **Results of the variational calculation for $\mathcal{H}_{\mathrm{TL}}$.** The parameters are fixed at $J = 0.032\,\mathrm{meV}$, $\Delta = 1.13$, $D/J = 3.97$, $g_c = 2.24$ and $B = 5\,\mathrm{T}$. **a** Comparison of the variational calculation at $M = 3$ and the exact results for the 2-magnon bound state. **b** Dispersion of the 3-magnon states at $M = 8$. **c** Dispersion of the 4-magnon states at $M = 8$. **d** Binding energies of the 2-, 3-, and 4-magnon states at different iterations.

Figure S19**d** shows no evidence that supports formation of 3-magnon bound state up to $M = 14$ iterations, and indicates that $E_3^B(\mathrm{K}) \to 0$ for $1/M \to 0$. In fact, the continuum of states in Fig. S19**b** already indicates that these are all scattering states between a 2-magnon bound state and a 1-magnon

state.

Similarly, the minimum of the 4-magnon state is located at Γ-point (Fig. S19**c**). The binding energy is defined by subtracting two 2-magnon bound states both at Γ:

$$E_4^B(\Gamma) = 2E_2(\Gamma) - E_4(\Gamma). \tag{S3}$$

Again, Figure S19**d** indicates that $E_4^B(\Gamma) \to 0$ for $1/M \to 0$. In other words, there is no formation of 4-magnon bound state. Note that the narrow continua of states below 1.72 meV in Fig. S19**c** are the scattering states of a pair of 2-magnon bound states.

X. DMRG CALCULATION

We use the same TL model as in the main text:

$$\mathcal{H}_{\mathrm{TL}} = J \sum_{\langle i,j \rangle} \left(S_i^x S_j^x + S_i^y S_j^y + \Delta S_i^z S_j^z \right) - D \sum_i \left(S_i^z \right)^2 - \widetilde{H} \sum_i S_i^z, \tag{S4}$$

where S_i^α ($\alpha = x, y, z$) are the spin-1 operators, and $\langle i, j \rangle$ runs over the nearest neighbor bonds. The anisotropies were fixed as $\Delta = 1.13$ and $D/J = 3.97$. In this section we set $J = 1$ as the unit of energy, and the results here should be scaled correspondingly for comparison to the main text. The effective magnetic field $\widetilde{H} \equiv g_c \mu_B B$ has already absorbed the g-factor g_c and the Bohr magneton μ_{B}.

The Hamiltonian (S4) was studied using a U(1) symmetric density matrix renormalization group (DMRG) method on long cylinders and torus. We first took $\widetilde{H} = 0$, and performed the ground state search procedure for every total spin quantum sector $S_z = \sum_i S_i^z$ on a $L_x \times L_y$ cylinder (y direction periodic, and x direction open) or torus, with $S_z \in [0, N]$, where $N = L_x L_y$ is the total number of

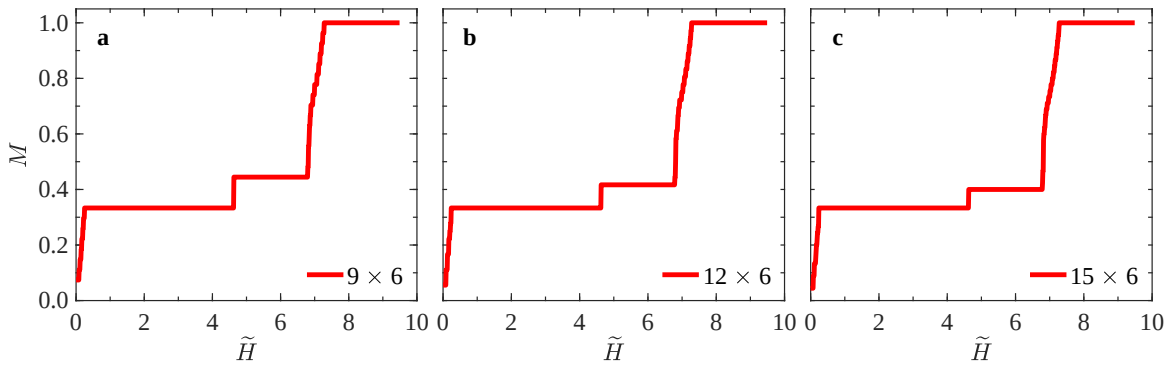

FIG. S20. Field dependence of the $T = 0$ magnetization for cylinders of size **a** 9×6, **b** 12×6, and **c** 15×6.

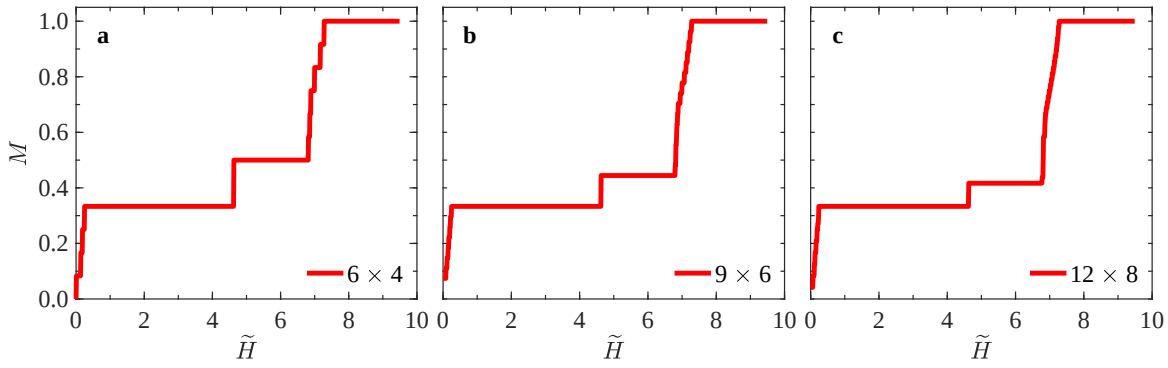

FIG. S21. Field dependence of the $T = 0$ magnetization for cylinders of size **a** 6×4, **b** 9×6, and **c** 12×8.

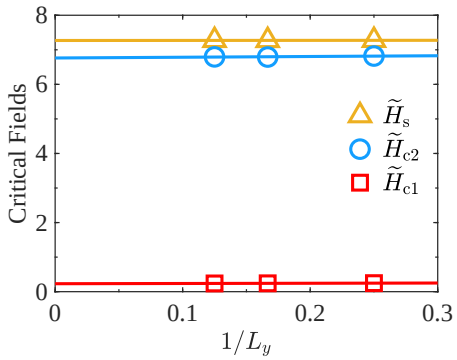

FIG. S22. Extrapolation of critical fields $\widetilde{H}_{\rm c1}$, $\widetilde{H}_{\rm c2}$, and $\widetilde{H}_{\rm s}$ as a function of $1/L_y$ to the thermodynamic limit, where linear regressions were used.

lattice sites. When external field $\widetilde{H} > 0$, the total energy of each spin sector S_z is shifted down by $\widetilde{H}S_z$ from its zero-field value, *i.e.*, $E(S_z, \widetilde{H}) = E(S_z, 0) - \widetilde{H}S_z$. The $T = 0$ magnetization can be obtained as $M = S_z^m/N$, where S_z^m is the total spin sector which takes the lowest energy among all sectors at any given $\widetilde{H}$. In other words, $E(S_z^m, \widetilde{H}) = \min\{E(S_z, \widetilde{H})\}$.

Besides the results on a torus presented in Fig. 5**a** in the main text, we computed the $T = 0$ magnetization curve on two series of cylinders. The first series involve cylinders of a fixed width $L_y = 6$ but different length $L_x = 9, 12, 15$. A maximum bond dimension of 1200 was used to ensure the convergence of the ground state energy at each quantum sector S_z. Ground state energy $E(S_z, 0)$ of each sector was extrapolated to zero discarded weight ϵ, defined as the sum of discarded eigenvalues of the reduced density matrix. In the worst cases, ϵ reaches 10^{-5}, and in other cases ϵ is around 10^{-8}. In Fig. S20, we show magnetization as a function of $\widetilde{H}$ for the 9×6, 12×6, and 15×6 cylinders. We find that all three sizes exhibit a wide $1/3$ plateau starting from $\widetilde{H}_{\rm c1} \approx 0.23$, ending around $\widetilde{H} = 4.8$. This $1/3$ plateau is followed by another "artificial" plateau whose magnetization M drops systematically with increasing L_x. We note that the total spin quantum number difference of the two neighboring plateaus is a constant ($\Delta S_z = L_y$) for any given L_y, therefore we believe that the "artificial" plateau will eventually merge into the $1/3$ plateau in the thermodynamic limit, whose range expands from $\widetilde{H}_{\rm c1} \approx 0.23$ to $\widetilde{H}_{\rm c2} \approx 6.76$. Following a narrow spin nematic phase for $\widetilde{H} \in [6.76, 7.27]$, the magnetization curve finally saturates when $\widetilde{H} \geq \widetilde{H}_{\rm s} \approx 7.27$.

In the second series of lattices, we increase the length L_x and the width L_y proportionally, using cylinders of size 6×4, 9×6, and 12×8. We aim at extrapolating the critical field strengths $\widetilde{H}_{\rm c1}$, $\widetilde{H}_{\rm c2}$, and $\widetilde{H}_{\rm s}$ accurately to the thermal dynamic limit. The maximum bond dimension used are

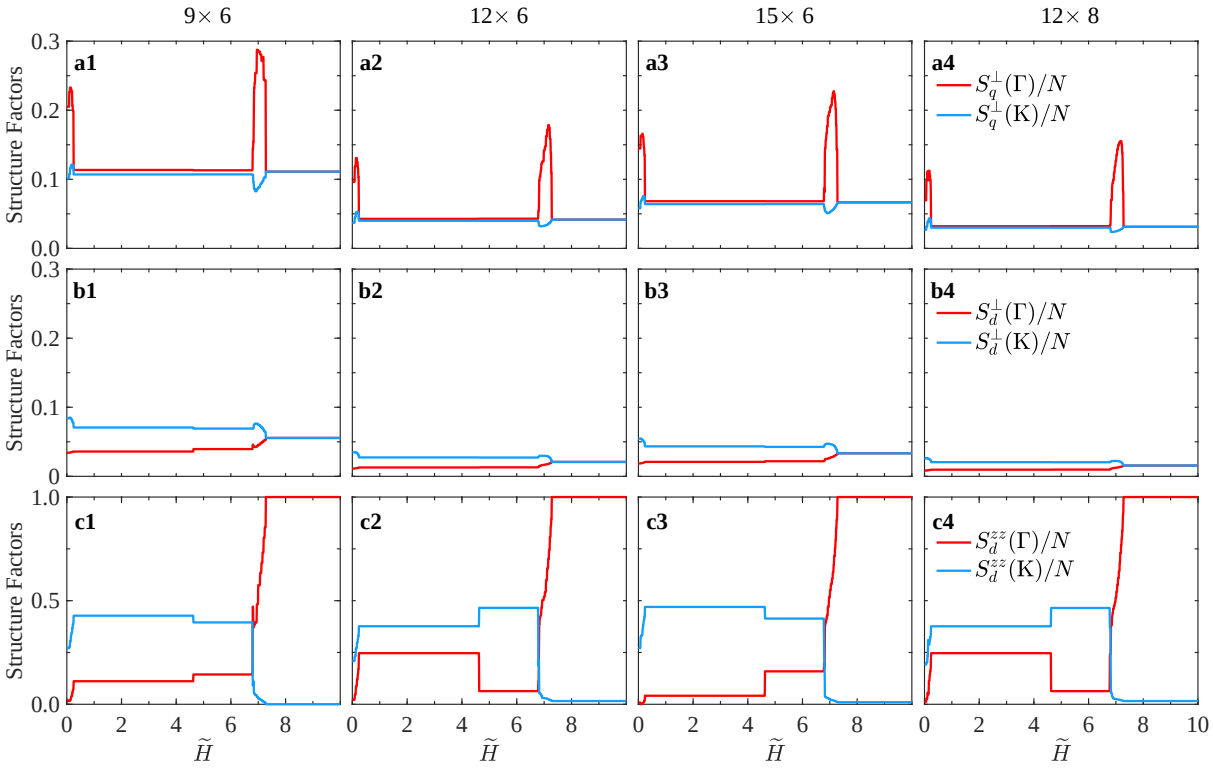

FIG. S23. **Dipolar and quadrupolar structure factors at Γ and K points. a** In-plane quadrupolar structure factor, **b** In-plane dipolar structure factor, **c** Out-of-plane dipolar structure factor. The corresponding lattice sizes are indicated on top of each column.

400 for 6×4, 1200 for 9×6, 3000 for 12×8 with the worst discarded weight reaches a scale of 10^{-5}. The magnetization curves of these three sizes are shown in Fig. S21. To our surprise, all critical fields $\widetilde{H}_{c1}$, $\widetilde{H}_{c2}$, and $\widetilde{H}_{s}$ have little finite size effects, and they extrapolate almost as a flat line in $1/L_y$ to the thermodynamic limit, as shown in Fig. S22. We conclude that $\widetilde{H}_{c1} = 0.230(8)$, $\widetilde{H}_{c2} = 6.76(3)$, and $\widetilde{H}_{s} = 7.270(4)$ in the thermodynamic limit. Here the error bars are defined by the largest absolute difference of the critical fields among different sizes. To compare with the experimental results, we convert $\widetilde{H}_{c1}$, $\widetilde{H}_{c2}$, and $\widetilde{H}_{s}$ to $B_{c1} = 0.057(2)\,\mathrm{T}$, $B_{c2} = 1.668(8)\,\mathrm{T}$ and $B_{s} = 1.794(1)\,\mathrm{T}$.

To reveal the nature of these phases, we computed the following structure factors:

$$S_d^{zz}(\boldsymbol{k}) = \frac{1}{N}\sum_{i,j} e^{-i\boldsymbol{k}\cdot(\boldsymbol{r}_i-\boldsymbol{r}_j)}\langle S_i^z S_j^z\rangle, \tag{S5a}$$

$$S_d^{\perp}(\boldsymbol{k}) = \frac{1}{N}\sum_{i,j} e^{-i\boldsymbol{k}\cdot(\boldsymbol{r}_i-\boldsymbol{r}_j)}\langle S_i^x S_j^x + S_i^y S_j^y\rangle, \tag{S5b}$$

$$S_q^{\perp}(\boldsymbol{k}) = \frac{1}{N}\sum_{i,j} e^{-i\boldsymbol{k}\cdot(\boldsymbol{r}_i-\boldsymbol{r}_j)}\langle Q_i^{x^2-y^2} Q_j^{x^2-y^2} + Q_i^{xy} Q_j^{xy}\rangle, \tag{S5c}$$

where $Q_i^{x^2-y^2} \equiv S_i^x S_i^x - S_i^y S_i^y$, $Q_i^{xy} \equiv S_i^x S_i^y + S_i^y S_i^x$. The labels i, j run over the center $\frac{1}{3}L_x \times L_y$ sites on a $L_x \times L_y$ cylinder, and for a torus they run over all the sites. The results for the torus can be found in Fig. 5**b** in the main text, that agree well with the perturbative calculations. Additional results on the cylinders are shown in Fig. S23, that also agree well with the ones on the torus. Due to limited system sizes available, we did not attempt to extrapolate the order parameters to the thermodynamic limit.

---

* These authors contributed equally to this work

† These authors contributed equally to this work; Corresponding author: meijw@sustech.edu.cn

‡ Corresponding author: Dehong.Yu@ansto.gov.au

§ Corresponding author: wuls@sustech.edu.cn

¶ Corresponding author: wan00351@umn.edu

[1] Li, N. *et al.* Quantum spin state transitions in the spin-1 equilateral triangular lattice antiferromagnet $Na_2BaNi(PO_4)_2$. *Phys. Rev. B* **104**, 104403 (2021). URL https://link.aps.org/doi/10.1103/PhysRevB.104.104403.

[2] Ding, F. *et al.* Structure and frustrated magnetism of the two-dimensional triangular lattice antiferromagnet $Na_2BaNi(PO_4)_2$. *Chinese Phys. B* **30**, 117505 (2021). URL https://doi.org/10.1088/1674-1056/abff1d.

[3] Zapf, V., Jaime, M. & Batista, C. D. Bose-Einstein condensation in quantum magnets. *Rev. Mod. Phys.* **86**, 563–614 (2014). URL https://link.aps.org/doi/10.1103/RevModPhys.86.563.

[4] Tanaka, H. *et al.* Magnetic quantum phase transitions from gapped spin liquid state in $TlCuCl_3$. *J. Magn. Magn. Mater.* **310**, 1343–1348 (2007). URL https://www.sciencedirect.com/science/article/pii/S0304885306015678.

[5] Trugman, S. A. Interaction of holes in a Hubbard antiferromagnet and high-temperature superconductivity. *Phys. Rev. B* **37**, 1597–1603 (1988). URL https://link.aps.org/doi/10.1103/PhysRevB.37.1597.

[6] Trugman, S. A. Spectral function of a hole in a Hubbard antiferromagnet. *Phys. Rev. B* **41**, 892–895 (1990). URL https://link.aps.org/doi/10.1103/PhysRevB.41.892.

[7] El Shawish, S. & Bonča, J. Spin-polaron excitations in a doped Shastry-Sutherland model. *Phys. Rev. B* **74**, 174420 (2006). URL https://link.aps.org/doi/10.1103/PhysRevB.74.174420.

[8] Haravifard, S. *et al.* In-Gap Spin Excitations and Finite Triplet Lifetimes in the Dilute Singlet Ground State System $SrCu_{2-x}Mg_x(BO_3)_2$. *Phys. Rev. Lett.* **97**, 247206 (2006). URL https://link.aps.org/doi/10.1103/PhysRevLett.97.247206.

[9] Wang, Z. & Batista, C. D. Dynamics and Instabilities of the Shastry-Sutherland Model. *Phys. Rev. Lett.* **120**, 247201 (2018). URL https://link.aps.org/doi/10.1103/PhysRevLett.120.247201.